



Co doping regulating electronic structure of Bi_2MoO_6 to construct dual active sites for photocatalytic nitrogen fixation

Chunming Yang, Yuanyuan Zhang, Feng Yue, Rui Du, Taoxia Ma, Yujie Bian, Ruqi Li, Li Guo^{*},
Danjun Wang^{*}, Feng Fu^{*}

Yan'an Key Laboratory of Green Catalysis and Quality Improvement and Utilization of Low Rank Coal, College of Chemistry & Chemical Engineering, Yan'an University, Yan'an 716000, PR China

ARTICLE INFO

Keywords:

Co doping
Electronic structure regulation
Dual active sites
N≡N bond adsorption/activation

ABSTRACT

Although photocatalytic nitrogen reduction reaction (PNRR) is a green ammonia synthesis technology, it still encounters low adsorption/activation efficiency of N_2 and lack of reaction active sites. Element doping is an efficient strategy to regulate electronic structure of catalyst. Nevertheless, the mechanism of the effect of doping elements on the N_2 adsorption/activation, reaction active site and energy barriers is not well unraveled. Taking Co doped Bi_2MoO_6 (Co- Bi_2MoO_6) as a model photocatalyst, density functional theory (DFT) and experiment study were used to investigate the mechanism of Co doping on the PNRR performance over Bi_2MoO_6 . DFT results reveal that Co doping regulates the electronic structure, activates Bi sites of Co- Bi_2MoO_6 and provides new Co active sites, thus constructing dual active sites for PNRR. Benefited from dual active sites for effectively adsorption/activation N_2 , the as-fabricated 3% Co- Bi_2MoO_6 exhibit the maximum NH_3 generation rate of $95.5 \mu\text{mol} \cdot \text{g}^{-1} \cdot \text{h}^{-1}$ without sacrificial agents, which is 7.2 times that of Bi_2MoO_6 . Furthermore, the detail mechanism of N≡N bond adsorption/activation and hydrogenation reaction on Co- Bi_2MoO_6 was also proposed according to in-situ FTIR and DFT results. This study provides a promising strategy to design catalysts with dual active sites for PNRR, which is of great significance to the popularization of other material systems.

1. Introduction

Ammonia (NH_3) is a decisive component of the commercial synthesis of fertilizers, refrigerants and military applications [1]. Besides, NH_3 is an ideal hydrogen storage material, as it can easily condense into liquid for storage. Accordingly, it is assumed that NH_3 may play an important role in hydrogen economy and can be used as the power of fuel cells to provide a good strategy to deal with the energy crisis [2–4]. Currently, industrial ammonia is produced through Haber-Bosch process, which is conditioned by high-purity nitrogen (N_2) and hydrogen (H_2) streams under high pressure (15–25 MPa) and high temperature (400–500 °C), consuming a large amount of energy and capital [5]. These shortcomings have widely aroused interest in developing sustainable and environment-friendly strategies of ammonia synthesis to reach the ambitious carbon peak and carbon neutrality objectives [6,7].

Photocatalytic nitrogen reduction reaction (PNRR) is an attractive way to substitute for Haber-Bosch's production of NH_3 as it utilizes the inexhaustible solar and water to directly provide electrons and protons

for N_2 hydrogenation to NH_3 , instead of supply high purity hydrogen [8,9]. The development of high-efficient PNRR catalysts has caused a range of research activities [10,11]. Unfortunately, most of currently developed photocatalytic materials still suffer from low adsorption/activation efficiency of N_2 and lack of reaction active sites, exhibiting limited conversion efficiencies for PNRR [12]. So far, numerous studies have been conducted to regulate the electronic structure of photocatalyst so as to optimize its nitrogen fixation performance [13]. Transitional metal element doping is widely used as an effective strategy to regulate the electronic structure to strengthen the N_2 adsorption/activation [14–17]. Xiong's group reported that Mo doping can efficiently enhance the N_2 adsorption/activation on the surface of $\text{W}_{18}\text{O}_{49}$ ultrathin nanowires, in which the coordinatively unsaturated metal atoms with oxygen defects serve as the sites for N_2 adsorption/activation [14]. Recently, Yin and co-workers created new active sites on MoS_2 for the adsorption of N_2 and dissociation of nonpolar $\text{N}\equiv\text{N}$ bond by Mn doping, in which the exposure of Mo edge sites is higher due to the formation of S vacancies [16]. Although the effect of element doping on regulation electronic structure

^{*} Corresponding authors.

E-mail addresses: guoli20052017@163.com (L. Guo), wangdj761118@163.com (D. Wang), yadxfufeng@126.com (F. Fu).

<https://doi.org/10.1016/j.apcatb.2023.123057>

Received 5 May 2023; Received in revised form 19 June 2023; Accepted 27 June 2023

Available online 28 June 2023

0926-3373/© 2023 Elsevier B.V. All rights reserved.

and creation of defective-type active sites of photocatalyst has been well researched, the effect of doped element on inherent active sites, as well as act as new active sites on N_2 adsorption/activation and energy barriers over photocatalyst is not well unraveled.

In this work, taking Co doped Bi_2MoO_6 (Co- Bi_2MoO_6) as a model photocatalyst, density functional theory (DFT) was used to investigate the effect of Co-doping on partial density of states (DOS), differential charge density and energy barrier of Bi_2MoO_6 . DFT results reveal that Co doping not only regulates the electronic structure, but also activates Bi sites of Co- Bi_2MoO_6 and provides new Co active sites, thus constructing dual active sites for PNRR. Under the guidance of DFT results, Co- Bi_2MoO_6 was synthesized by a facile solvothermal process. Ascribed to Co-doping regulated the electronic structure of Bi_2MoO_6 to construct dual active sites for effectively adsorption/activation N_2 , the as-fabricated 3% Co- Bi_2MoO_6 achieved the maximum NH_3 generation rate of $95.5 \mu\text{mol}\cdot\text{g}^{-1}\cdot\text{h}^{-1}$ under visible light irradiation without sacrificial agents, which is 7.2 times that of Bi_2MoO_6 . Furthermore, the detail steps for $N\equiv N$ bond adsorption/activation and hydrogenation reaction pathway on Co- Bi_2MoO_6 are depicted according to DFT and in-situ FTIR results. This study provides fresh insights into design catalysts with dual active sites for PNRR and reaffirms the versatility of subtle electronic structure modulation in tuning catalytic activity.

2. Experimental and computational section

2.1. Preparation of Bi_2MoO_6

Pure Bi_2MoO_6 was prepared by solvothermal method. Typically, under intense stirring, 1.94 g of $Bi(NO_3)_3\cdot 5H_2O$ (4 mmol) and 0.484 g of $Na_2MoO_4\cdot 2H_2O$ (2 mmol) were dissolved in a mixed solution of glycol (40 mL) and ethanol (10 mL) to obtain transparent liquid and transfer to a 65 mL autoclave lined with polytetrafluoroethylene for solvothermal reaction at 190 °C for 2 h. The yellow precipitation was then separated, washed with ethanol and deionized water for several times, and dried to obtain Bi_2MoO_6 product.

2.2. Preparation of Co- Bi_2MoO_6

The Co- Bi_2MoO_6 photocatalyst was prepared by hydrothermal method. In a typical process, 40 mL of $0.0005 \text{ mol}\cdot\text{L}^{-1}$ $CoCl_2\cdot 6H_2O$ solution was taken into a 100 mL beaker, and 1 g of Bi_2MoO_6 was added to the solution, and stirred for 1 h. Finally, the homogeneous solution was transferred into a 65 mL Teflon-lined stainless steel autoclave and maintained at 160 °C for 5 h. The product was separated by centrifugation, washed with ethanol and deionized water for several times and then dried overnight. The obtained product was marked as 0.5% Co- Bi_2MoO_6 . The change in $CoCl_2\cdot 6H_2O$ (0.001, 0.002, 0.003, 0.004, 0.006 $\text{mol}\cdot\text{L}^{-1}$) concentration was used to create a series of samples for experimental optimization, which were referred to as X% Co- Bi_2MoO_6 (X = 0.5, 1, 2, 3, 4, 6, X means the mass ratio of $CoCl_2\cdot 6H_2O$ and Bi_2MoO_6).

2.3. Photocatalysis nitrogen reduction reaction

The photocatalytic activity of nitrogen fixation was evaluated under visible light. Generally, in a quartz reaction, add photocatalyst (100 mg) to ultrapure water (150 mL). Before irradiation, to eliminate dissolved oxygen, the suspension was rapidly agitated in the dark for 30 min and bubbled in high purity nitrogen. During irradiation, 7 mL of solution was taken out every 30 min, and then centrifuged at 11000 rpm for 5 min to remove photocatalyst for the following NH_3/NH_4^+ concentration analysis.

2.4. Theoretical calculations

The DOS, differential charge density and energy barrier of Bi_2MoO_6

and Co- Bi_2MoO_6 were performed through the spin-polarized density functional theory (DFT) as implemented by the Vienna ab initio simulation package (VASP). Perdew-Burke-Ernzerhof (PBE) generalized gradient approximation (GGA) was used to describe the exchange-correlation energy functional. Projected augmented wave (PAW) pseudopotential was used for depicting the ion core and the periodic boundary condition. Spin polarization was also considered. A 2×1 supercell, three layers of pristine Bi_2MoO_6 (010) and Co- Bi_2MoO_6 (010) surface were chosen to construct the investigated models. Geometry optimizations, DOS, differential charge density and free energy were performed with a convergence threshold of 10^{-5} eV in energy and 0.05 eV/Å for the force. A vacuum of 15 Å along the z-direction was used, which was large enough to minimize the interactions between periodic images. The free energy of PNRR was calculated by using the equation:

$$\Delta G = E_{\text{surface+adsorbate}} - E_{\text{surface}} - E_{\text{adsorbate}} + \Delta E_{\text{ZPE}} - T\Delta S,$$

where G, E, ZPE and TS represent the free energy, total energy from DFT calculations, zero point energy and entropic contributions, respectively.

3. Results and discussion

3.1. DFT calculation for catalysts design

The key step in the PNRR process is known to be adsorption/activation of N_2 on catalyst surface. During the N_2 adsorption/activation process, the electrons on bonding orbital (highest occupied molecule orbital, HOMO, $2\sigma_g$) of N_2 interact with the d-orbital of catalyst active site to form the adsorption state. Then the d-orbital electrons of catalyst active site feedback to anti-bonding orbital (lowest unoccupied molecule orbital, LUMO, $1\pi_g$) of the N_2 to activate the $N\equiv N$ bond to form N_2 active state ($\cdot N_2$), and then $\cdot N_2$ reacts with the H^+ and photo-generated electrons to form NH_3 (Fig. 1a). Hence, it is crucial that catalytic active site provide symmetric orbit matching with the anti-bonding orbital of the N_2 .

Bismuth molybdate (Bi_2MoO_6) is a typical Aurivillius oxide, composed of a layered structure with alternate stacking of $(Bi_2O_2)^{2+}$ sheets interleaved with $[MoO_4]^{2-}$ layer [18]. The hybridization of Bi 6s and O 2p orbit constitute its valence band (VB), Mo 4d ($4d^5$) constitute its conduction band (CB) (Fig. 1b and c) [19,20]. Thermodynamic, the energy band structure of Bi_2MoO_6 meets the potential requirement of the PNRR [21]. Theoretically, the structure of Bi_2MoO_6 determines that Bi sites (Bi_2MoO_6 -Bi) is responsible for N_2 molecule adsorption/activation other than Mo sites in the PNRR. Nevertheless, the Bi 6s orbit is difficult to form adsorption states with the N_2 molecules. The Co atoms possesses ideal d-band electronic structure ($3d^7$) that spatially matches the anti-bonding orbital of N_2 [22]. As shown in Fig. 1d, the high overlap of N, Bi, and Co peaks in the PDOS indicates that the Co- Bi_2MoO_6 is propitious to accept electrons from N_2 HOMO ($2\sigma_g$) to form adsorbed state N_2 , and then electrons transfer from the Co d-orbital to the anti-bonding orbital (LUMO, $1\pi_g$) of $N\equiv N$ to activate N_2 . Furthermore, Co doping induces an impurity energy level near the top of Bi_2MoO_6 valence band, which is beneficial for electron excitation [23]. According to the differential charge density (Fig. 1e), it is clear that the electrons transfer from d-orbital Co sites (Co- Bi_2MoO_6 -Co) to the anti-bonding orbital of adsorbed N_2 . Therefore, the essence of the N_2 adsorption/activation on the surface of transition metal site (Co and Bi) is the “acceptance donation” of electrons, where the electron structure of d orbitals determines the energy barriers of PNRR.

The DFT calculations were further performed to gain insight into the effect of Co doping on N_2 adsorption/activation as well as reveal inherent mechanism of PNRR activity [24–26]. Fig. 2a exhibited the d-orbital DOS of Co- Bi_2MoO_6 and Bi_2MoO_6 to examine the influence of Co doping on the electronic structure. The d-band centers of Co- Bi_2MoO_6 and Bi_2MoO_6 are -3.1 and -2.7 eV, respectively. Co-doping resulted in shifting up d-band center of Bi_2MoO_6 , which may be in favor of

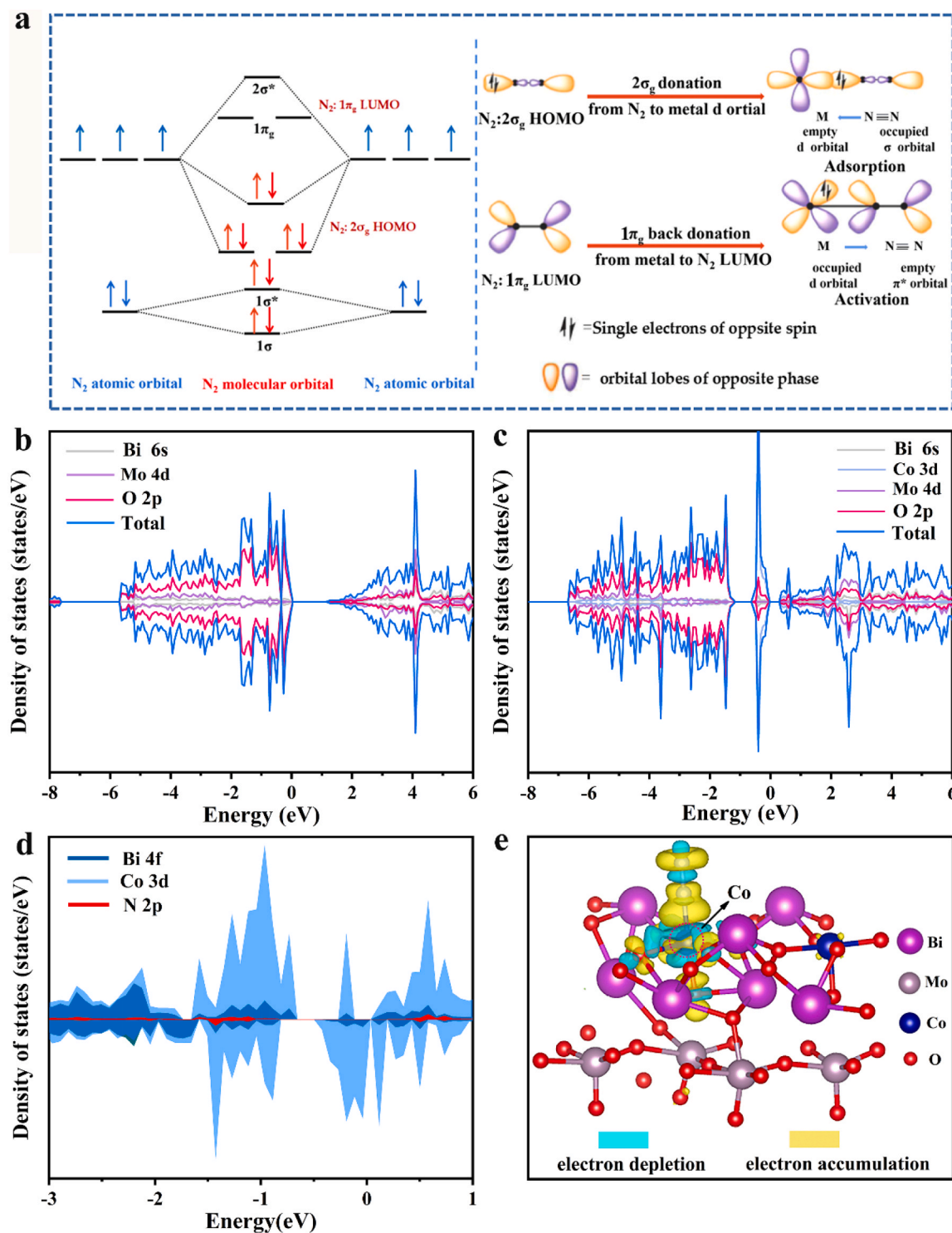


Fig. 1. (a) Schematic of N_2 bond adsorption/activation process. The calculated DOS of (b) Bi_2MoO_6 , (c) $\text{Co-Bi}_2\text{MoO}_6$ and (d) $\text{Co-Bi}_2\text{MoO}_6$ with adsorbed N_2 . (e) Differential charge densities for $\text{Co-Bi}_2\text{MoO}_6\text{-Co}$ with adsorbed N_2 .

physical/chemical adsorption, activation and hydrogenation of N_2 molecule [25]. The Gibbs free energy of N_2 adsorption was calculated to identify the adsorption/activation ability of photocatalyst. The adsorption free energy of N_2 on $\text{Bi}_2\text{MoO}_6\text{-Bi}$ and on Bi sites in $\text{Co-Bi}_2\text{MoO}_6$ ($\text{Co-Bi}_2\text{MoO}_6\text{-Bi}$) are -0.2 and -0.44 eV, respectively (Fig. 2b), indicating that Co doping can activate Bi sites ($\text{Co-Bi}_2\text{MoO}_6\text{-Bi}$) and improve its adsorption/activation ability. Simultaneously, the adsorption free energy for N_2 on Co sites ($\text{Co-Bi}_2\text{MoO}_6\text{-Co}$) is -0.59 eV, manifesting

that Co can be considered as the main adsorption sites during PNRR. Additionally, materials with enhanced adsorption performance correspond to weakened $\text{N}\equiv\text{N}$ triple bonds. As shown in Fig. 2b, the $\text{N}\equiv\text{N}$ lengths of $\text{Co-Bi}_2\text{MoO}_6\text{-Co}$, $\text{Co-Bi}_2\text{MoO}_6\text{-Bi}$ are 1.132 and 1.118 Å, respectively, which exhibit significant elongations compared with that of Bi_2MoO_6 (1.117 Å).

To explore the entire reaction path of synthetic ammonia over $\text{Co-Bi}_2\text{MoO}_6$, this process was determined by calculating the Gibbs free

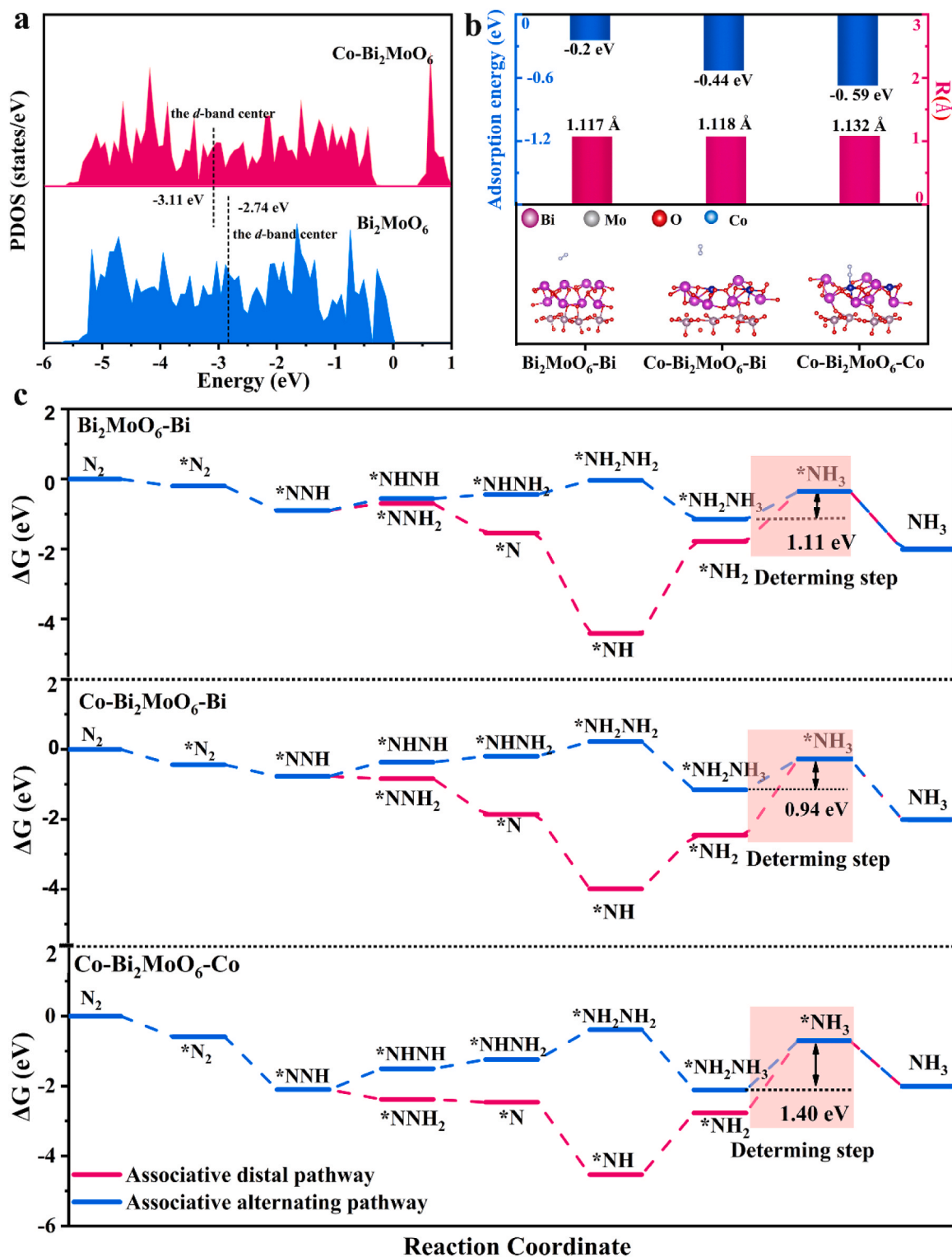


Fig. 2. (a) PDOS and d-band center calculation using the PBE method of Bi_2MoO_6 and $\text{Co-Bi}_2\text{MoO}_6$. (b) Calculated adsorption free energy and $\text{N}\equiv\text{N}$ lengths of N_2 on $\text{Bi}_2\text{MoO}_6\text{-Bi}$, $\text{Co-Bi}_2\text{MoO}_6\text{-Bi}$ and $\text{Co-Bi}_2\text{MoO}_6\text{-Co}$ sites. (c) Gibbs free energy diagram for N_2 reduction over Bi_2MoO_6 , $\text{Co-Bi}_2\text{MoO}_6\text{-Bi}$ and $\text{Co-Bi}_2\text{MoO}_6\text{-Co}$ sites.

energy (Fig. 2c and Fig. S1) [27]. Associative alternating pathway and associative distal pathway share the same initial hydrogenation step ($\text{*N}_2 + \text{H}^+ + \text{e}^- \rightarrow \text{*N-NH}$), but the succeeding hydrogenation stages vary because of different processes [28]. Three kinds of active sites ($\text{Bi}_2\text{MoO}_6\text{-Bi}$, $\text{Co-Bi}_2\text{MoO}_6\text{-Bi}$, $\text{Co-Bi}_2\text{MoO}_6\text{-Co}$) follow the associative alternating pathway because the associative distal pathway exhibit the higher energy barriers. The rate-determining step ($\text{*NH}_2\text{NH}_3 \rightarrow \text{*NH}_3$)

energy barriers of associative alternating pathway are 1.11, 0.94 and 1.4 eV, respectively. Although the rate-determining step energy barrier of $\text{Co-Bi}_2\text{MoO}_6\text{-Co}$ is relatively high, it possesses the strongest N_2 adsorption capacity among the three kinds of active sites. Since N_2 adsorption/activation is the key step of the PNRR, the $\text{Co-Bi}_2\text{MoO}_6\text{-Co}$ sites also act as active sites of PNRR as well as $\text{Co-Bi}_2\text{MoO}_6\text{-Bi}$ sites. Theoretically, Co doping regulates the electronic structure of Bi_2MoO_6 ,

activates the Co-Bi₂MoO₆-Bi sites, provides the new Co-Bi₂MoO₆-Co active sites, thus constructing dual active sites for PNRR.

3.2. Characterization of catalysts

Inspired by the theoretical results, we fabricated Bi₂MoO₆ and Co-Bi₂MoO₆ by a solvothermal method (Fig. S2). X-ray diffraction (XRD) was used to analyze the crystalline structures of Bi₂MoO₆ and Co-Bi₂MoO₆ with different Co contents. All diffraction peaks of Bi₂MoO₆ conformed to the orthorhombic Bi₂MoO₆ structure (JCPDS No.76-2388) (Fig. 3a). Additionally, the peak intensity of (131) and (002) planes in Bi₂MoO₆ decreased with the increase of cobalt content and no new peaks were detected in the XRD patterns of Co-Bi₂MoO₆. The enlarged XRD patterns in the range of 25–35° indicated the characteristic peaks (131) and (002) gradually shift to the higher angle. Since the atomic radius of Co was smaller than that of Bi, it was certain that the Bi atoms in the main crystal were partially replaced by Co atoms (Fig. 3b) [29,30].

X-ray photoelectron spectroscopy (XPS) was employed to reveal the chemical valence of Bi₂MoO₆ and 3% Co-Bi₂MoO₆ (Fig. 3c-f and Fig. S3). As shown in Fig. 3c, the binding energy of Bi appeared at 159.12 and 164.43 eV in 3% Co-Bi₂MoO₆ could be attributed to Bi 4f_{7/2} and Bi 4f_{5/2} respectively, indicating that Bi exists in the form of Bi³⁺ [31]. The binding energy of Mo 3d in 3% Co-Bi₂MoO₆ (232.39 and 235.53 eV) was in accordance with Mo 3d_{3/2} and Mo 3d_{5/2} of Mo⁶⁺ (Fig. 3d) [32]. The binding energy of Bi 4f and Mo 3d peaks is slightly higher than that of Bi₂MoO₆, indicating that the electron cloud density around Bi and Mo is decreased due to the doping of Co²⁺. Considering that Co (1.7) has a bigger Alley-Luo Zhou electronegativity than Bi (1.67) and Mo (1.30), the substitution of Bi³⁺ by Co²⁺ may cause bonding electrons to accumulate on Co²⁺, decreasing the electron cloud density of Bi and Mo elements and increasing the binding energy. The O 1s of Bi₂MoO₆ and Co-Bi₂MoO₆ exhibited two characteristic peaks, the binding energy of 529.82 and 530.7 eV was attributed to lattice oxygen (Bi-O, Mo-O) and adsorbed oxygen, respectively (Fig. 3e) [33,34]. For 3% Co-Bi₂MoO₆,

two characteristic peaks of Co 2p at 780.99 and 805.33 eV belong to Co 2p_{3/2} and Co 2p_{1/2} indicate the chemical state of Co²⁺ (Fig. 3f) [35].

The morphology of Bi₂MoO₆ and 3% Co-Bi₂MoO₆ was investigated using scanning electron microscope (SEM) and transmission electron microscope (TEM), as shown in Fig. S4 and Fig. 4. Both Bi₂MoO₆ and Co-Bi₂MoO₆ exhibited spherical structure with an average diameter of about 3–5 μm (Fig. 4a and d). Furthermore, the HRTEM image clearly displayed lattice stripes of Bi₂MoO₆ and 3% Co-Bi₂MoO₆ at (131) plane raised from 0.315 to 0.335 nm (Fig. 4c and f) [36]. The energy dispersive X-ray (EDX) mapping further proved that 3% Co-Bi₂MoO₆ was composed of Bi, Mo, O and Co elements (Fig. 4g).

3.3. Nitrogen fixation performance

Pure water and pure nitrogen were employed as feedstocks, without adding sacrificial reagent, the PNRR activity of Bi₂MoO₆ and Co-Bi₂MoO₆ was carried out under visible light ($\lambda > 420$ nm) and simulated sunlight irradiation, respectively. The generated ammonia (NH₃/NH₄⁺) was measured by Nessler's reagent method (Fig. S5). As shown in Fig. 5a, the NH₃/NH₄⁺ yield of Bi₂MoO₆ was approximately 10 μmol·g⁻¹·h⁻¹ under visible light. After Co was doped into Bi₂MoO₆, the PNRR activity was significantly improved. Meanwhile, it manifested a volcano-type activity in NH₃/NH₄⁺ yield, which was a function of Co content. Particularly, the 3% Co-Bi₂MoO₆ exhibited the highest NH₃/NH₄⁺ yield rate of up to 95.5 μmol·g⁻¹·h⁻¹, which was 7.2-fold higher than that of the Bi₂MoO₆ and was prominent in the reported literatures (Table S1). While further increasing the Co doping content, the PNRR activity of Co-Bi₂MoO₆ decreased due to the excessive Co doping leading to lower separation efficiency of photo-generated e⁻/h⁺ pairs. The as-produced ammonia source was testified by the isotope labeling experiment. ¹⁵N₂ and ¹⁴N₂ with high purity were used as feed gases. As shown in ¹H nuclear magnetic resonance spectroscopy (NMR) (Fig. 5b), when ¹⁴N₂ was introduced into the PNRR experiment, the split triplet state of the ¹⁴NH₄⁺ signal appeared. Nevertheless, two symmetrical splitting

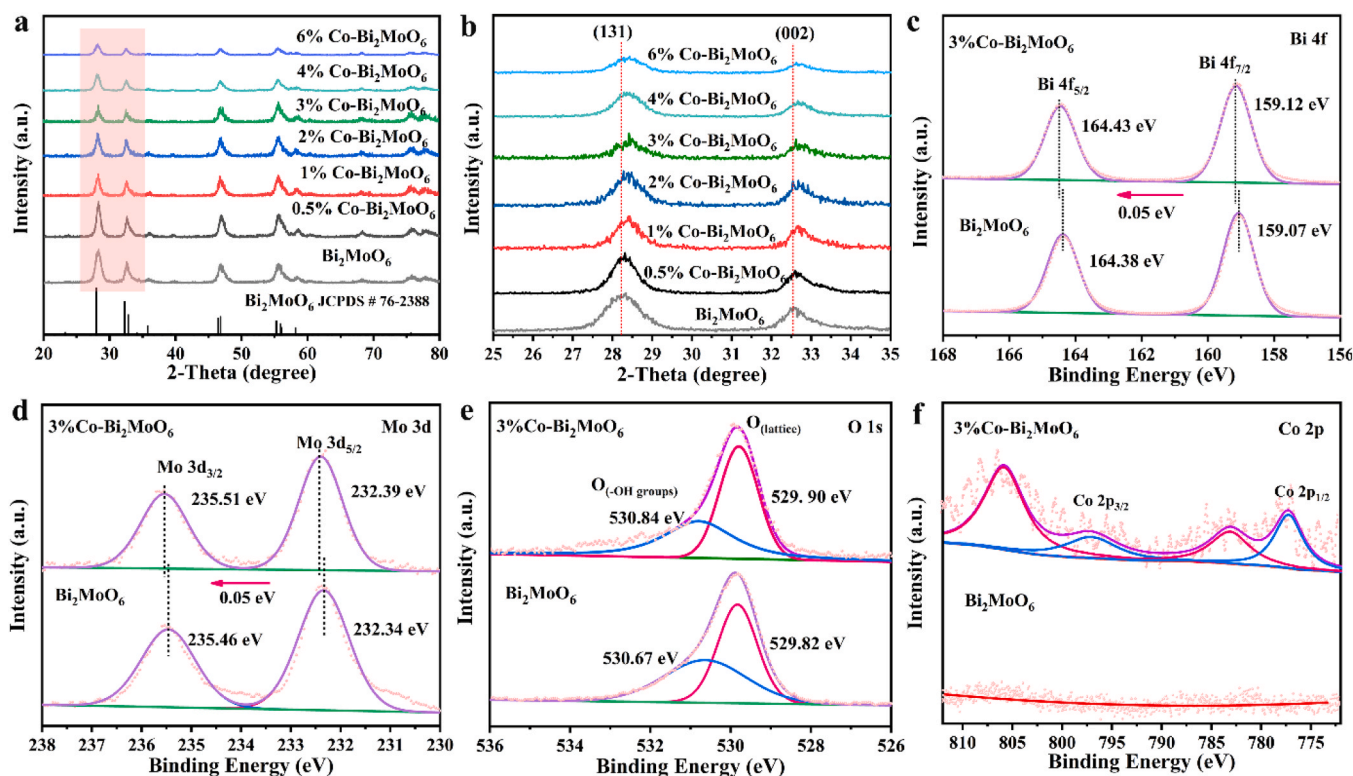


Fig. 3. (a) XRD patterns of Bi₂MoO₆ and Co-Bi₂MoO₆. (b) Magnified patterns of (131) and (002) crystal plane of Bi₂MoO₆ and Co-Bi₂MoO₆ in the range of 25–35° and XPS spectra of (c) Bi 4f, (d) Mo 3d, (e) O 1s and (f) Co 2p for Bi₂MoO₆ and 3% Co-Bi₂MoO₆.

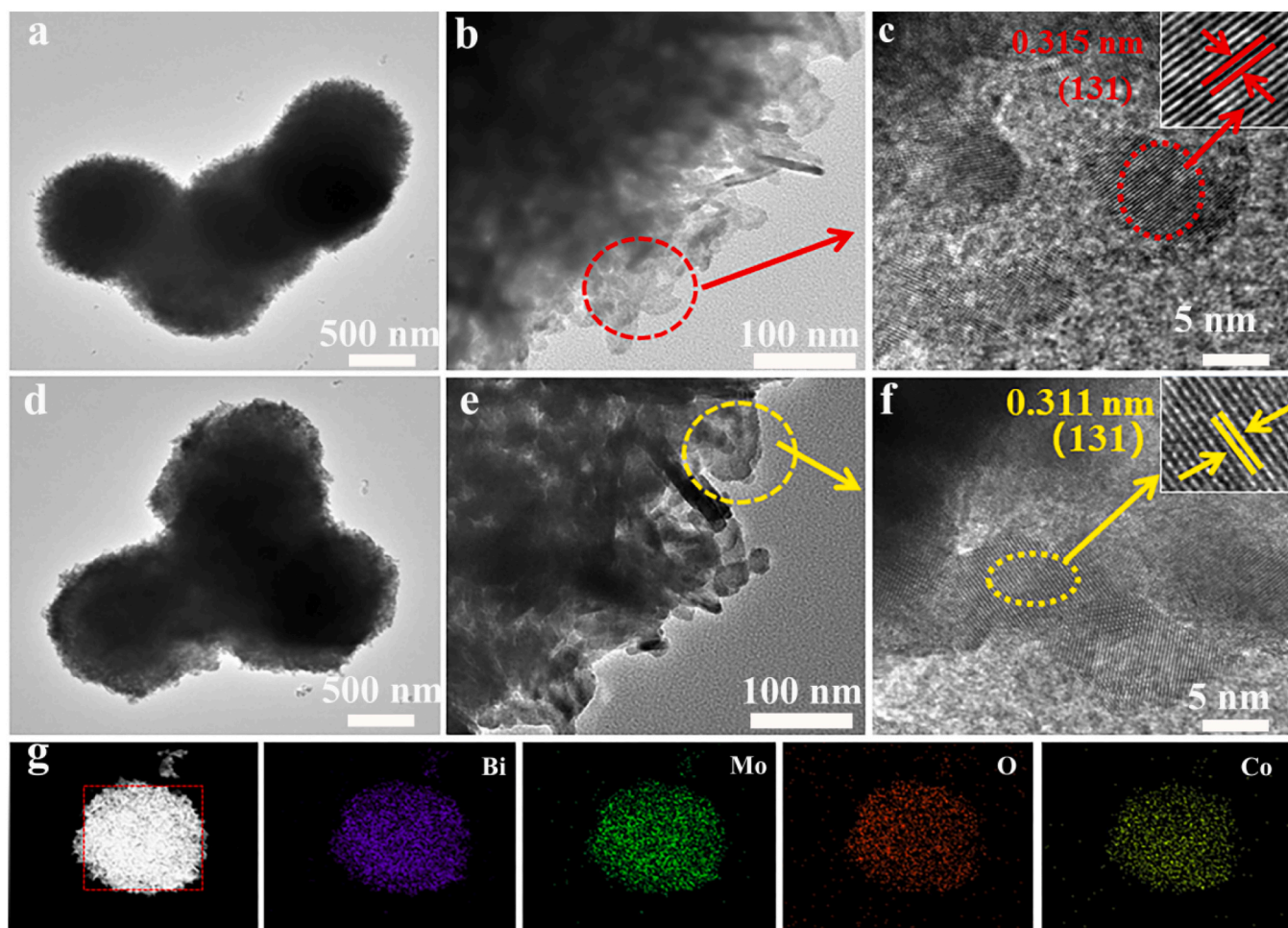


Fig. 4. TEM images of (a–b) Bi_2MoO_6 , (d–e) 3% $\text{Co-Bi}_2\text{MoO}_6$. (c, f) HRTEM images of Bi_2MoO_6 and 3% $\text{Co-Bi}_2\text{MoO}_6$, respectively. (g) EDX-mapping containing Bi, Mo, O and Co elements.

peaks of $^{15}\text{NH}_4^+$ were obviously observed when used $^{15}\text{N}_2$, which may be relevant to the coupling between ^1H resonance and ^{15}N , and in good agreement with the standard ^{15}N signal [37]. These results strongly verified that the ammonia produced indeed originated from N_2 fixation reaction rather than other nitrogen impurities.

To evaluate the light utilization efficiency, the apparent quantum efficiency (AQE) of 3% $\text{Co-Bi}_2\text{MoO}_6$ irradiated by monochromatic light was also measured (Fig. 5c). The AQE of 3% $\text{Co-Bi}_2\text{MoO}_6$ is in accordance with UV–vis diffuse reflectance spectrum, which indicates that it had high utilization efficiency of incident light. Specifically, with the increase of monochromatic light wavelength (i.e., 365, 380, 400, 420, 450, 500 and 550 nm), AQE decreased (1.009%, 0.806%, 0.561%, 0.224%, 0.172%, 0.074% and 0.02%). Moreover, the controllable experiments revealed that 3% $\text{Co-Bi}_2\text{MoO}_6$ do not produce ammonia under Ar atmosphere or dark conditions, indicating that the $\text{NH}_3/\text{NH}_4^+$ produced by 3% $\text{Co-Bi}_2\text{MoO}_6$ in pure H_2O under N_2 atmosphere and light irradiation was the result of PNRR (Fig. 5d). The ion chromatography (IC) was also used for detecting the produced $\text{NH}_3/\text{NH}_4^+$, which was quantified to be about $103 \mu\text{mol} \cdot \text{g}^{-1} \cdot \text{h}^{-1}$ (Fig. S6), matching the value determined by the Nessler's reagent method.

It should be noted that there were negligible by-products N_2H_4 and NO_3^- , indicating the high selectivity of $\text{NH}_3/\text{NH}_4^+$ (Fig. S7 and S8) [38]. Furthermore, the cycling experiments indicated that 3% $\text{Co-Bi}_2\text{MoO}_6$ has a relatively stable ammonia production rate during 5 cycles (Fig. S9). Moreover, the crystal structure of $\text{Co-Bi}_2\text{MoO}_6$ after PNRR was investigated, as shown in Fig. S10. The XRD revealed that no phase significant difference occurred for 3% $\text{Co-Bi}_2\text{MoO}_6$ before and after

illumination, further confirming its great PNRR stability.

3.4. Nitrogen fixation mechanism investigation

To further investigate the mechanism for the enhanced PNRR activity of 3% $\text{Co-Bi}_2\text{MoO}_6$, the energy band structure and the carrier dynamics were systematically analyzed. The UV–vis diffuse reflectance absorption spectra (UV–Vis DRS) indicates that the absorption threshold of $\text{Co-Bi}_2\text{MoO}_6$ presented red-shift, indicating that Co doping broadens the absorption range of Bi_2MoO_6 (Fig. 6a). On the basis of the Tauc curves by Kubelka-Munk equation, the calculated band gap (E_g) of Bi_2MoO_6 and 3% $\text{Co-Bi}_2\text{MoO}_6$ were determined to be 2.52 and 2.39 eV, respectively (insert picture in Fig. 6a). The conduction band minimum (CBM) of Bi_2MoO_6 and 3% $\text{Co-Bi}_2\text{MoO}_6$ was estimated according to Mott-Schottky curve. It indicated that the curve slopes of Bi_2MoO_6 and 3% $\text{Co-Bi}_2\text{MoO}_6$ were both positive, confirming both of them were n-type semiconductors, and the flat band potentials (E_{fb} vs. NHE) are -0.36 and -0.43 V vs NHE, respectively (Fig. 6b). It is well-accepted that the conduction band potential of n-type is closed to its flat band potential [39]. Thus, the CBM values of Bi_2MoO_6 and 3% $\text{Co-Bi}_2\text{MoO}_6$ were estimated to be -0.36 and -0.43 V, respectively. According to the empirical formula ($E_g = E_{\text{VBM}} - E_{\text{CBM}}$), the valance band maximum (VBM) values of Bi_2MoO_6 and 3% $\text{Co-Bi}_2\text{MoO}_6$ were calculated to be 2.16 and 1.96 V vs NHE, respectively, which were consistent with the valance band XPS results (Fig. 6c). Fig. 6d depicted the band gap structure of Bi_2MoO_6 and 3% $\text{Co-Bi}_2\text{MoO}_6$ and the standard reduction potential of some chemicals. It should be noted that the potentials of the

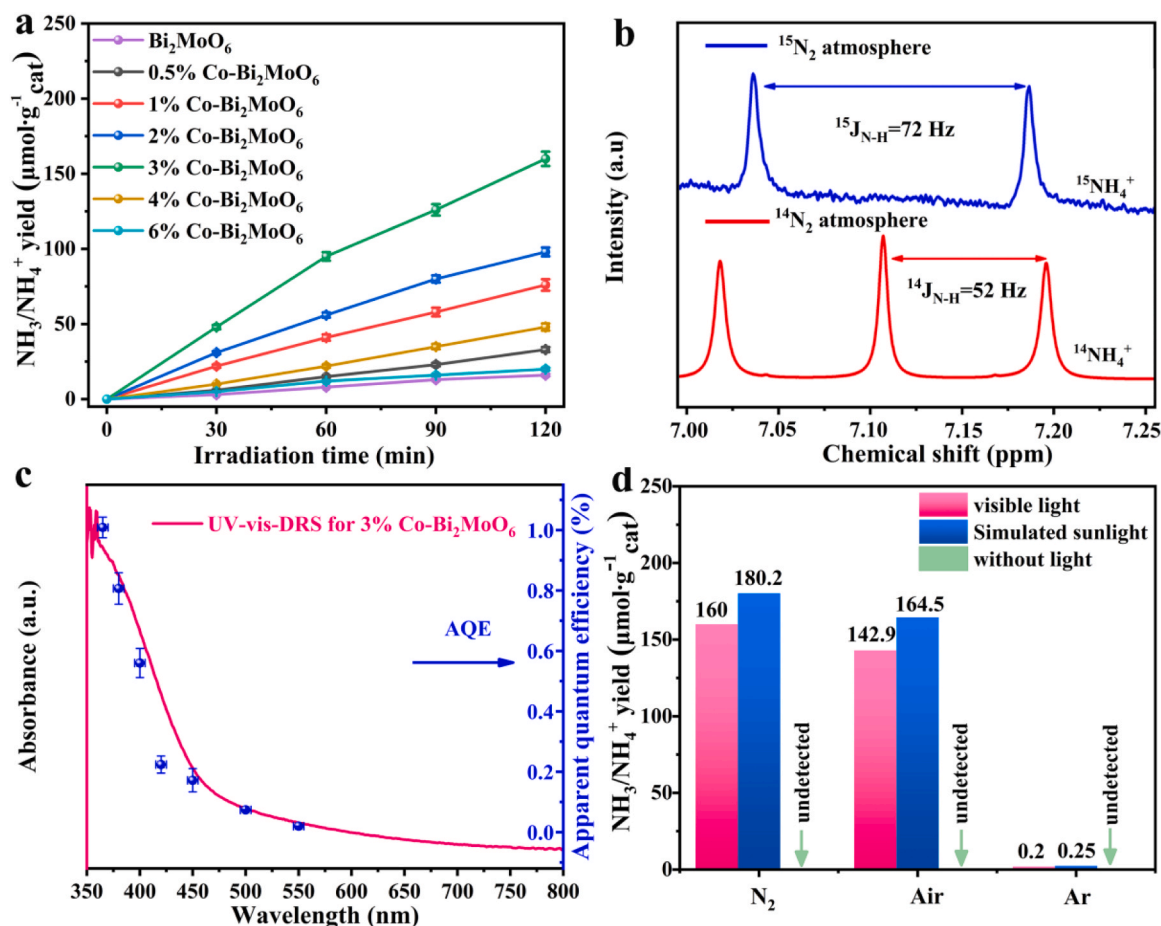


Fig. 5. (a) Photocatalytic N₂ fixation performance of Bi₂MoO₆ and Co-Bi₂MoO₆ under visible light. (b) ¹H NMR spectrum for produced NH₄⁺ using N₂ (¹⁵N₂ and ¹⁴N₂) and water as feedstock. (c) Calculated AQEs for PNRR over 3% Co-Bi₂MoO₆ under monochromatic light irradiation. (d) Comparison of 3% Co-Bi₂MoO₆ with different nitrogen sources under visible light and simulated sunlight, respectively.

CBM and the VBM can drive the PNRR half-reaction and the water oxidation half-reaction, respectively ($E_{CBM} < \varphi_{N_2}$, $H^+/NH_3 < \varphi_{N_2}$ and $E_{VBM} > \varphi_{O_2}$, H^+/H_2O) [40]. Therefore, Co-Bi₂MoO₆ had more negative conduction band and excellent nitrogen reduction performance, which is conducive to improve PNRR activity.

The electrochemical performance of the Bi₂MoO₆ and 3% Co-Bi₂MoO₆ was studied by transient photocurrent and electrochemical impedance spectra (EIS), which provided the information of charge separation and transfer dynamics of photocatalyst [41]. As shown in Fig. 7a and Fig. S11, Co doping can obviously increase the photocurrent density of Bi₂MoO₆, implying that the Co doping can improve the separation of carriers efficiency. Nevertheless, the excessive doped Co may act as the recombination centre which lead to the recombination of photogenerated e^-/h^+ . The charge transfer resistance at the FTO/catalyst (R_1) and the catalyst/electrolyte interface (R_2) was calculated according to the Nyquist plots [42]. As shown in Fig. 7b, after Co doping, the R_2 was decreased from 3555 Ω to 1391 Ω, indicating that Co-Bi₂MoO₆ had lower charge-transfer resistance. These results suggested that 3% Co-Bi₂MoO₆ possess better charge separation efficiency than Bi₂MoO₆, implying its higher carrier transfer dynamics at the photocatalyst/solution interface. The photoluminescence (PL) intensity of 3% Co-Bi₂MoO₆ was lower than Bi₂MoO₆, indicating that Co doping can hinder the recombination of photogenerated carriers (Fig. 7c). The decay dynamics was also observed from time-resolved fluorescence decay spectroscopy (Fig. 7d). It revealed that carrier lifetime of 3% Co-Bi₂MoO₆ (2.78 ns) was longer than that of Bi₂MoO₆ (2.16 ns), implying that carrier migration and transportation had been improved.

The nitrogen temperature-programmed desorption (N₂-TPD)

indicated that physisorption/chemisorption peaks of 3% Co-Bi₂MoO₆ were stronger than those of Bi₂MoO₆, reflecting an improvement in 3% Co-Bi₂MoO₆ adsorption and activation capacity for N₂ (Fig. 8a), thus significantly improving the activation of N₂ molecule and PNRR performance [43]. Furthermore, in-situ FTIR was employed to further investigate the progress of adsorption/activation and hydrogenation on the surface of 3% Co-Bi₂MoO₆ (Fig. 8b). During the PNRR process, a number of oscillation bands can be easily distinguished after the dark adsorption equilibrium. The peak I at 3385 cm⁻¹ was related to N-H stretching mode. The characteristic absorption peaks of NH₄⁺ and NH₃ were assigned to the peak II (2882 cm⁻¹), peak V (1403 cm⁻¹) and peak IV (1557 cm⁻¹), respectively [44,45]. The characteristic absorption peak of the *N₂ was corresponded to the peak III located at 1649 cm⁻¹ [46]. Additionally, the intensity of peaks II and V increased with the extension of irradiation time. It is worth noting that two characteristic vibrations of hydrazine were not observed at 1290 and 1129 cm⁻¹ [46].

Furthermore, the formation of superoxide radicals ($\bullet O_2^-$) was investigated by in-situ ESR technique, which can indirectly testify the oxidation half-reaction in the process of PNRR ($H_2O + h\nu_{VB} \rightarrow H^+ + O_2 + e^-$). As shown in Fig. 9, the $\bullet O_2^-$ produced by 3% Co-Bi₂MoO₆ in the atmosphere of Ar, air and N₂ were monitored and studied with dimethylpyridine nitrogen oxide (DMPO) as the scavenger. The typical EPR signal of DMPO- $\bullet O_2^-$ of 3% Co-Bi₂MoO₆ gradually increased, proving the production of O₂ and the formation of $\bullet O_2^-$ due to the capturing the conduction band electrons of the catalyst by oxygen molecules ($O_2 + e^- \rightarrow \bullet O_2^-$). Under the visible light irradiation, the concentration of DMPO- $\bullet O_2^-$ adduct produced by 3% Co-Bi₂MoO₆ was much higher than that of Bi₂MoO₆, which indicates that 3% Co-Bi₂MoO₆ produced more active

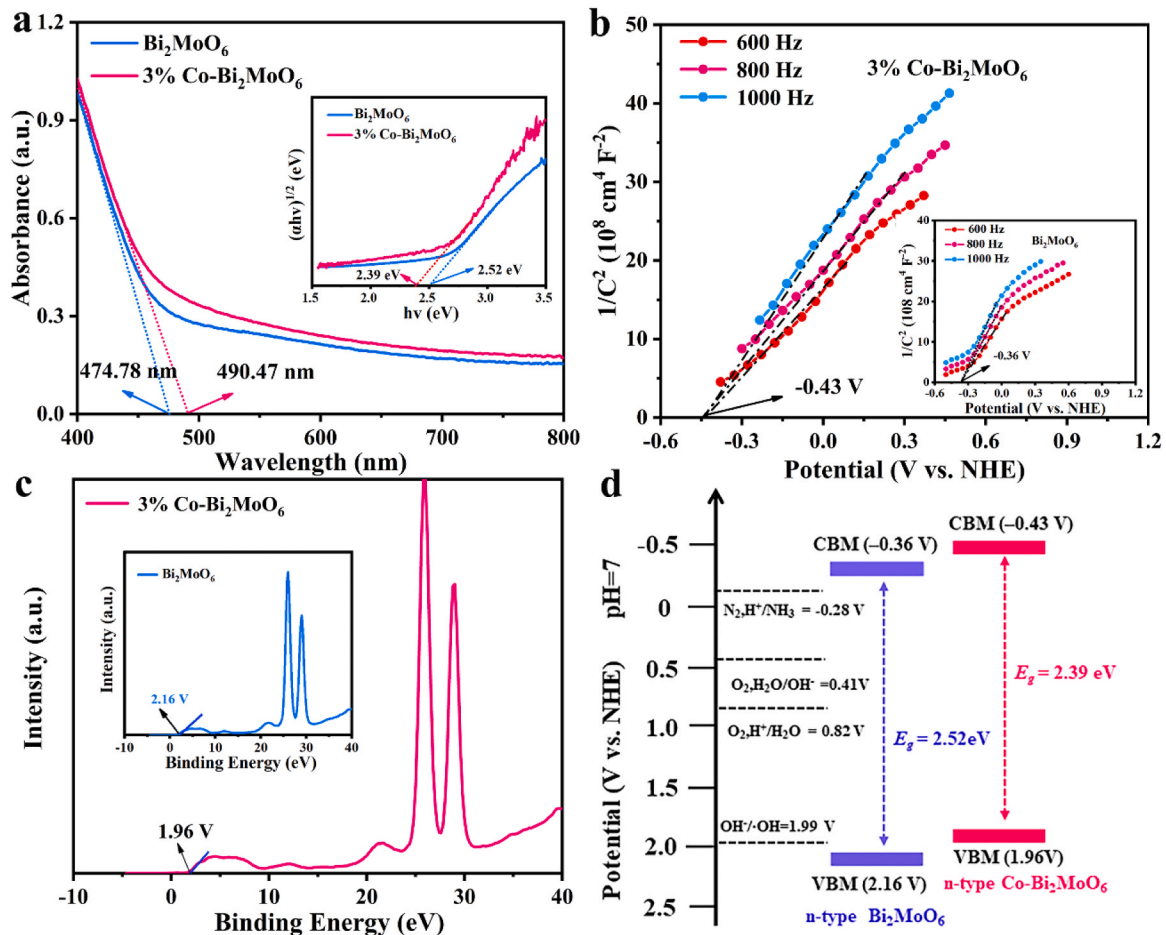


Fig. 6. (a) UV-vis DRS spectra of Bi_2MoO_6 and 3% $\text{Co-Bi}_2\text{MoO}_6$ (the inset shows corresponding Tauc plots $[(F(R)h\nu)^{1/2}]$ versus photon energy ($h\nu$)). (b) Mott-Schottky plots of Bi_2MoO_6 (inset) and 3%- $\text{Co-Bi}_2\text{MoO}_6$ under different alternating current potential frequency. (c) Valence band XPS spectrum of Bi_2MoO_6 (inset) and 3%- $\text{Co-Bi}_2\text{MoO}_6$. (d) Schematic illustration of the band structure for Bi_2MoO_6 and 3% $\text{Co-Bi}_2\text{MoO}_6$.

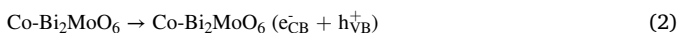
radicals (Fig. S12).

Fig. 10 shows a schematic of the PNRR mechanism on $\text{Co-Bi}_2\text{MoO}_6$ with dual active sites using N_2 and H_2O as feedstock without sacrificial agents (Eq. 1), which mainly involves the following steps: i) Under light irradiation, electrons are excited from the VBM of $\text{Co-Bi}_2\text{MoO}_6$ to CBM, h^+ are generated in VBM. The produced e^-/h^+ pairs transferred to the surface of the photocatalyst, where the photocatalytic N_2 fixation occurs (Eq. 2). ii) The adsorption state N_2 ($^*\text{N}_2$) was formed on Co and Bi dual active sites via the interaction with N_2 ($2\delta_g$, HOMO) and unoccupied orbitals of $\text{Co-Bi}_2\text{MoO}_6$ (Eq. 3). iii) The orbital electrons of Co and Bi active sites feedback to anti-bonding orbital ($1\pi_g$, LUMO) of N_2 to activate the $\text{N}\equiv\text{N}$ bond, achieving the N_2 active state ($\cdot\text{N}_2$) (Eq. 4). iv) H_2O is oxidized by the h^+_{VB} to produce O_2 and release H^+ and e^- (Eq. 5). Simultaneously, O_2 capture e^-_{CB} to produce $\cdot\text{O}_2$, which was testified by In-situ ESR (Fig. 9) (Eq. 6). v) The $\cdot\text{N}_2$ reacts with the H^+ and e^-_{CB} to form NH_3 (Eq. 7).

Overall reaction:

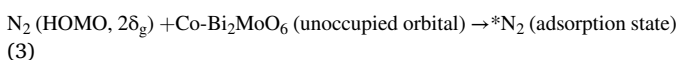


Step 1: Carrier generation and spatial separation.

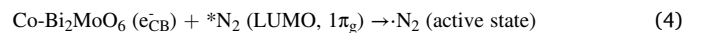


Step 2: N_2 adsorption/activation on Co and Bi active sites.

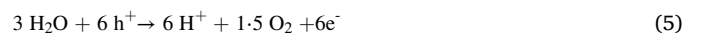
N_2 adsorption:



$\text{N}\equiv\text{N}$ bond activation:



Step 3: Water oxidation half-reaction to produce O_2 and release H^+ and e^-



Step 4: Photocatalytic NRR half-reaction to produce NH_3 .



4. Conclusion

In summary, based on the DFT calculation, Co doping regulates the electronic structure of Bi_2MoO_6 , activates Bi sites of Co doped Bi_2MoO_6 ($\text{Co-Bi}_2\text{MoO}_6$) and provides new Co active sites, thus constructing dual active sites for PNRR. We successfully construct $\text{Co-Bi}_2\text{MoO}_6$ photocatalyst with dual active sites to investigate the effect of Co doping on the adsorption/activation and hydrogenation reaction. The as-prepared 3% $\text{Co-Bi}_2\text{MoO}_6$ exhibit the maximum NH_3 generation rate of $95.5 \mu\text{mol}\cdot\text{g}^{-1}\cdot\text{h}^{-1}$ without sacrificial agents, which is 7.2 times that of Bi_2MoO_6 . These performance enhancements can be attributed to the following: i) Co doping induces an impurity energy level near the top of Bi_2MoO_6 valence band, which is beneficial for accelerating the

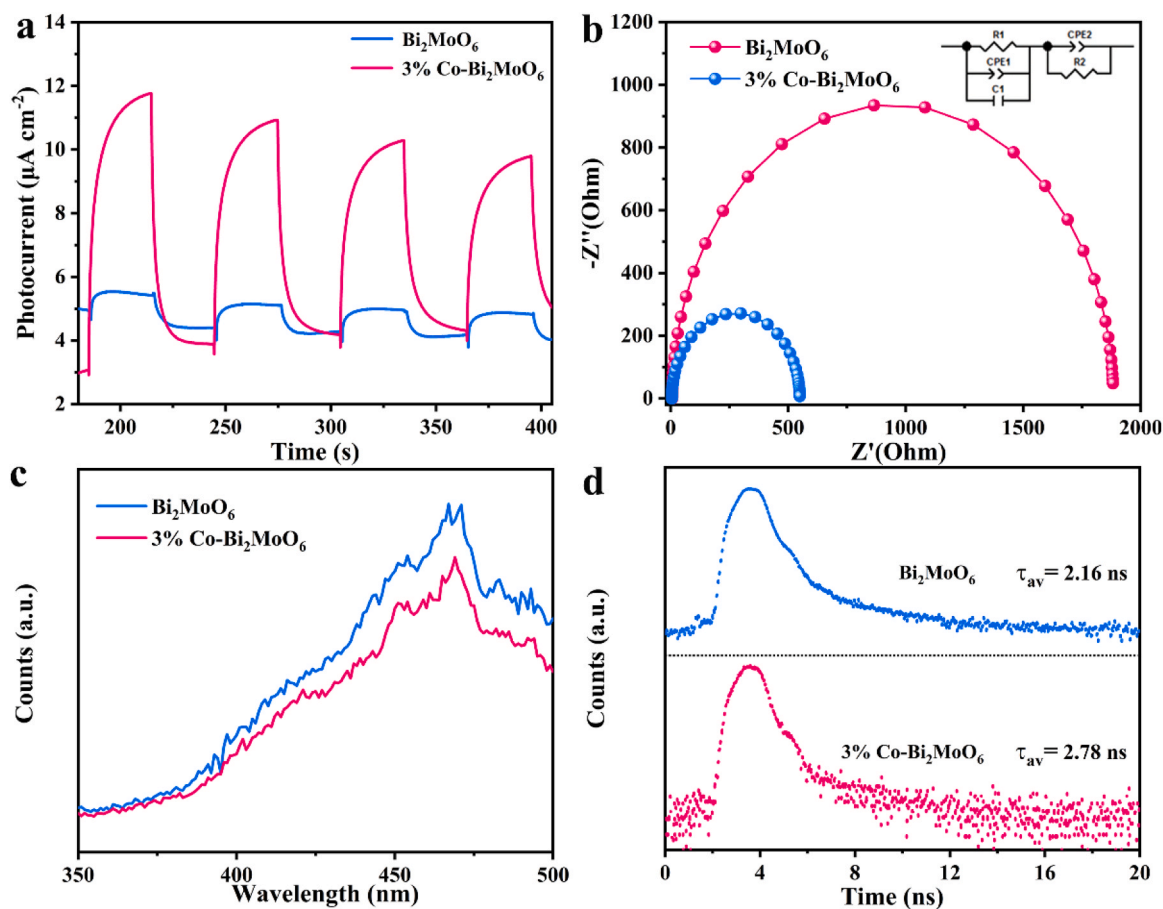


Fig. 7. (a) Photocurrent response plots, (b) Nyquist plots, (c) The room temperature PL spectra ($\lambda_{\text{excitation}} = 270 \text{ nm}$) and (d) Time-resolved fluorescence decay spectra of Bi_2MoO_6 and 3% $\text{Co-Bi}_2\text{MoO}_6$.

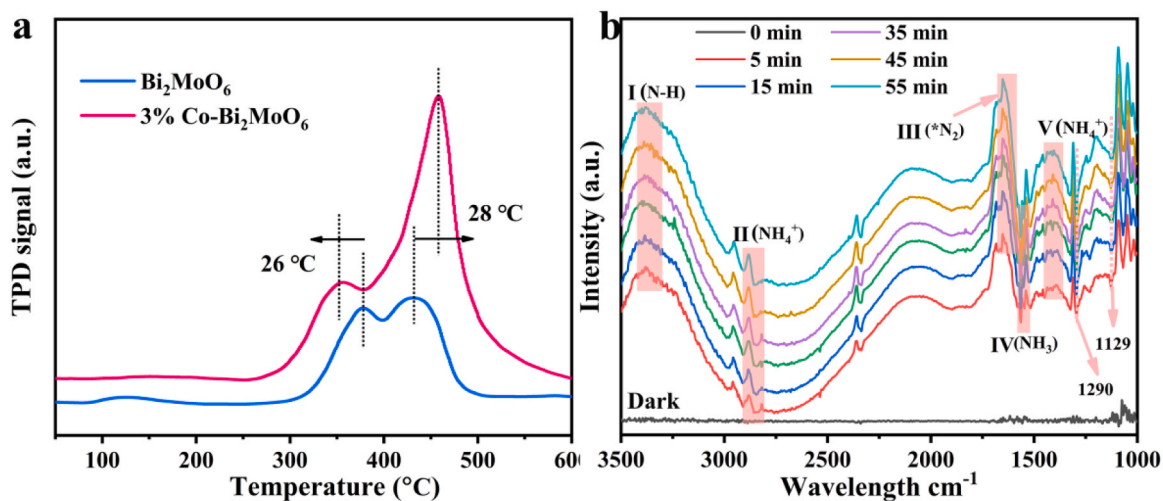


Fig. 8. (a) N_2 -TPD profiles of the as-prepared Bi_2MoO_6 and 3% $\text{Co-Bi}_2\text{MoO}_6$. (b) In-situ FTIR spectra of N_2 fixation on 3% $\text{Co-Bi}_2\text{MoO}_6$ for up to 55 min's photoirradiation.

separation/transformation dynamics of carrier as well as enhancing the redox ability of Bi_2MoO_6 . ii) Co doping regulates the electronic structure of Bi_2MoO_6 , activates the $\text{Co-Bi}_2\text{MoO}_6\text{-Bi}$ sites, provides the new $\text{Co-Bi}_2\text{MoO}_6\text{-Co}$ active sites, thus constructing dual active sites for PNRR. Finally, the boosted mechanism of PNRR on $\text{Co-Bi}_2\text{MoO}_6$ with dual active sites was also proposed according to in-situ FTIR and DFT results. The present study provides a promising reference for combination of

DFT and experiment to design and construct high-efficiency nitrogen fixation photocatalysts.

CRediT authorship contribution statement

Chunming Yang: Methodology, Data curation, Writing. **Yuanyuan Zhang:** Methodology, Data curation. **Feng Yue:** Methodology, Data

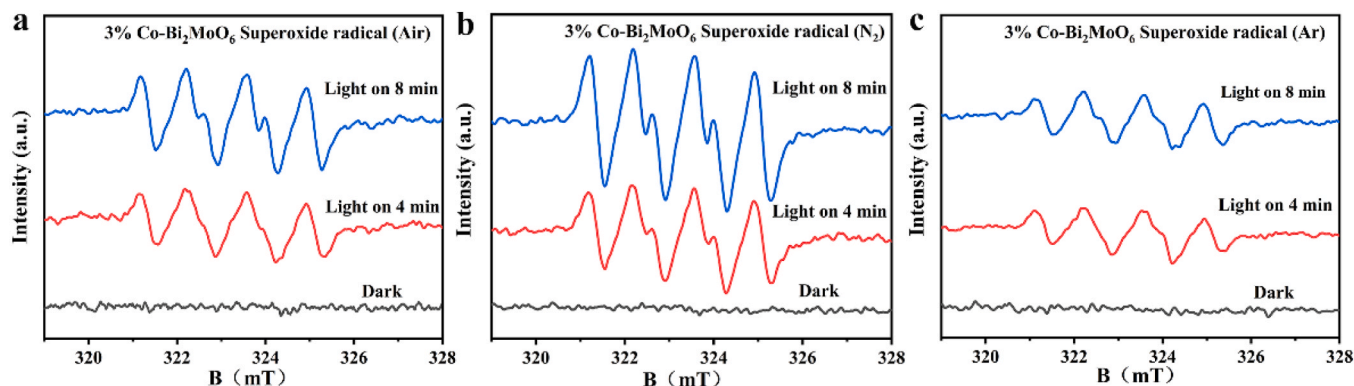


Fig. 9. DMPO spin-trapping ESR spectra of $\bullet\text{O}_2$ of (a) air, (b) N_2 and (c) Ar recorded with visible light irradiation of 3% Co-Bi₂MoO₆.

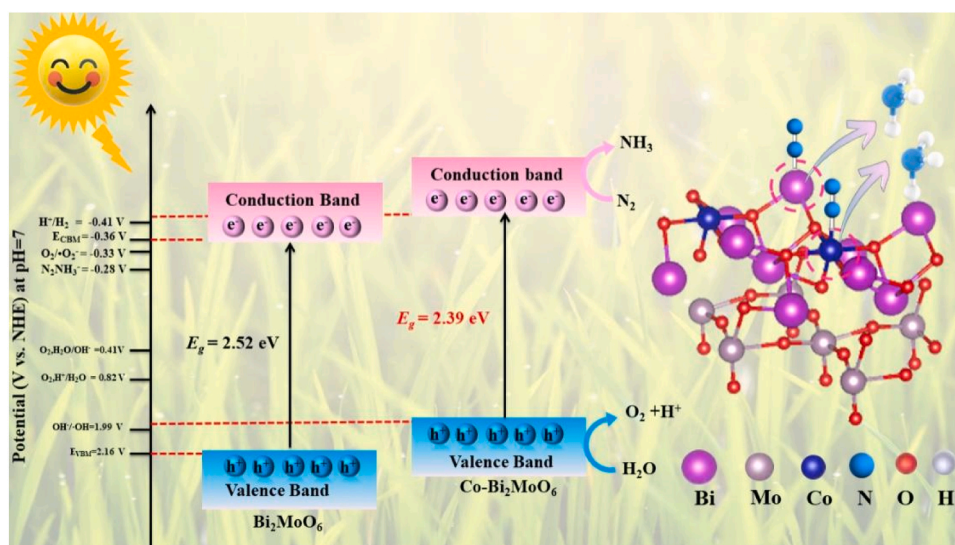


Fig. 10. Schematic of the PNRR mechanism on 3% Co-Bi₂MoO₆ with dual active sites under illumination.

curation. **Rui Du**: Investigation, Validation. **Taoxia Ma**: Investigation, Data curation. **Yujie Bian**: Review & editing. **Ruqi Li**: Validation, Review & editing. **Li Guo**: Resources, Validation, Review & editing. **Danjuan Wang**: Conceptualization, Writing – review & editing, Funding acquisition. **Feng Fu**: Validation, Resources, Supervision.

Declaration of Competing Interest

The authors declare that they have no known competing financial interests or personal relationships that could have appeared to influence the work reported in this paper.

Data availability

Data will be made available on request.

Acknowledgements

This work was financially supported by the National Natural Science Foundation of China (No.22168040, 22162025) and the Project of Science & Technology Office of Shaanxi Province (No.2022JM-062).

Appendix A. Supporting information

Supplementary data associated with this article can be found in the online version at [doi:10.1016/j.apcatb.2023.123057](https://doi.org/10.1016/j.apcatb.2023.123057).

References

- [1] J.A. Pool, E. Lobkovsky, P.J. Chirik, Hydrogenation and cleavage of dinitrogen to ammonia with a zirconium complex, *Nature* 427 (2004) 527–530.
- [2] Y. Dong, T. Wang, S. Hu, Y. Tang, X. Hu, Y. Ye, H. Li, D. Cao, Electrochemical reduction of N_2 into NH_3 under ambient conditions using Ag-doped TiO₂ Nanofibers, *ACS Appl. Nano Mater.* 4 (2021) 10370–10377.
- [3] G. Jiang, Z. Li, L. Mou, S. He, Dual iron sites in activation of N_2 by iron–sulfur cluster anions Fe_5S_2 and Fe_5S_3 , *J. Phys. Chem. Lett.* 12 (2021) 9269–9274.
- [4] W. Zhang, Y. Shen, F. Pang, D. Quek, W. Niu, W. Wang, P. Chen, Facet-dependent catalytic performance of Au nanocrystals for electrochemical nitrogen reduction, *ACS Appl. Mater. Interfaces* 12 (2020) 41613–41619.
- [5] S. Wang, F. Ichihara, H. Pang, H. Chen, J. Ye, Nitrogen fixation reaction derived from nanostructured catalytic materials, *Adv. Funct. Mater.* 28 (2018), 1803309.
- [6] X. Chen, N. Li, Z. Kong, W. Ong, X. Zhao, Photocatalytic fixation of nitrogen to ammonia: state-of-the-art advancements and future prospects, *Mater. Horiz.* 5 (2018) 9–27.
- [7] C. Lv, Y. Qian, C. Yan, Y. Ding, Y. Liu, G. Chen, G. Yu, Defect engineering metal-free polymeric carbon nitride electrocatalyst for effective nitrogen fixation under ambient conditions, *Angew. Chem.* 130 (2018) 10403–10407.
- [8] R. Guan, D. Wang, Y. Zhang, C. Liu, W. Xu, J. Wang, Z. Zhao, M. Feng, Q. Shang, Z. Sun, Enhanced photocatalytic N_2 fixation via defective and fluoride modified TiO₂ surface, *Appl. Catal. B: Environ.* 282 (2021), 119580.
- [9] C. Hu, X. Chen, J. Jin, Y. Han, S. Chen, H. Ju, J. Cai, Y. Qiu, C. Gao, C. Wang, Surface plasmon enabling nitrogen fixation in pure water through a dissociative mechanism under mild conditions, *J. Am. Chem. Soc.* 141 (2019) 7807–7814.
- [10] G. Zhang, C.D. Sewell, P. Zhang, H. Mi, Z. Lin, Nanostructured photocatalysts for nitrogen fixation, *Nano Energy* 71 (2020), 104645.
- [11] Y. Fu, Y. Liao, P. Li, H. Li, S. Jiang, H. Huang, W. Sun, T. Li, H. Yu, K. Li, Layer structured materials for ambient nitrogen fixation, *Coord. Chem. Rev.* 460 (2022), 214468.

- [12] B. Sun, S. Lu, Y. Qian, X. Zhang, J. Tian, Recent progress in research and design concepts for the characterization, testing, and photocatalysts for nitrogen reduction reaction, *Carbon Energy* 5 (2023), e305.
- [13] Y. Bo, H. Wang, Y. Lin, T. Yang, R. Ye, Y. Li, C. Hu, P. Du, Y. Hu, Z. Liu, Altering hydrogenation pathways in photocatalytic nitrogen fixation by tuning local electronic structure of oxygen vacancy with dopant, *Angew. Chem. Int. Ed.* 60 (2021) 16085–16092.
- [14] N. Zhang, A. Jalil, D. Wu, S. Chen, Y. Liu, C. Gao, W. Ye, Z. Qi, H. Ju, C. Wang, X. Wu, L. Song, J. Zhu, Y. Xiong, Refining defect states in $\text{W}_{18}\text{O}_{49}$ by Mo doping: a strategy for tuning N_2 activation towards solar-driven nitrogen fixation, *J. Am. Chem. Soc.* 140 (2018) 9434–9443.
- [15] X. Chen, X. Zhang, Y. Li, M. Qi, J. Li, Z. Tang, Z. Zhou, Y. Xu, Transition metal doping BiOBr nanosheets with oxygen vacancy and exposed {102} facets for visible light nitrogen fixation, *Appl. Catal. B: Environ.* 281 (2021), 119516.
- [16] B. Hu, B. Wang, Z. Bai, L. Chen, J. Guo, S. Shen, T. Xie, C. Au, L. Jiang, S. Yin, Regulating MoS_2 edge site for photocatalytic nitrogen fixation: a theoretical and experimental study, *Chem. Eng. J.* 442 (2022), 136211.
- [17] K. Li, W. Cai, Z. Zhang, H. Xie, Q. Zhong, H. Qu, Boron doped C_3N_5 for photocatalytic nitrogen fixation to ammonia: the key role of boron in nitrogen activation and mechanism, *Chem. Eng. J.* 435 (2022), 135017.
- [18] H. Yu, L. Jiang, H. Wang, B. Huang, X. Yuan, J. Huang, J. Zhang, G. Zeng, Modulation of Bi_2MoO_6 -based materials for photocatalytic water splitting and environmental application: a critical review, *Small* 15 (2019), 1901008.
- [19] X. Liu, S. Gu, Y. Zhao, G. Zhou, W. Li, BiVO_4 , Bi_2WO_6 and Bi_2MoO_6 photocatalysis: a brief review, *J. Mater. Sci. Technol.* 56 (2020) 45–68.
- [20] X. Yang, X. Xu, J. Wang, T. Chen, S. Wang, X. Ding, H. Chen, Insights into the surface/interface modifications of Bi_2MoO_6 : feasible strategies and photocatalytic applications, *Sol. RRL* 5 (2021), 2000442.
- [21] Y. Zhang, L. Guo, Y. Wang, T. Wang, T. Ma, Z. Zhang, D. Wang, B. Xu, F. Fu, In-situ anion exchange based $\text{Bi}_2\text{S}_3/\text{OV-Bi}_2\text{MoO}_6$ heterostructure for efficient ammonia production: a synchronized approach to strengthen NRR and OER reactions, *J. Mater. Sci. Technol.* 110 (2022) 152–160.
- [22] V.G. Pershina, Electronic structure and properties of the transactinides and their compounds, *Chem. Rev.* 96 (1996) 1977–2010.
- [23] T. Liu, G. Tan, C. Zhao, C. Xu, Y. Su, Y. Wang, H. Ren, A. Xia, D. Shao, S. Yan, Enhanced photocatalytic mechanism of the Nd-Er co-doped tetragonal BiVO_4 photocatalysts, *Appl. Catal. B: Environ.* 213 (2017) 87–96.
- [24] F. Xu, K. Meng, S. Cao, C. Jiang, T. Chen, J. Xu, J. Yu, Step-by-step mechanism insights into the $\text{TiO}_2/\text{Ce}_2\text{S}_3$ S-scheme photocatalyst for enhanced aniline production with water as a proton source, *ACS Catal.* 12 (2021) 164–172.
- [25] D.K. Yesudoss, H. Chun, B. Han, S. Shanmugam, Accelerated N_2 reduction kinetics in hybrid interfaces of NbTiO_4 and nitrogen-doped carbon nanorod via synergistic electronic coupling effect, *Appl. Catal. B: Environ.* 304 (2022), 120938.
- [26] W. Guo, K. Zhang, Z. Liang, R. Zou, Q. Xu, Electrochemical nitrogen fixation and utilization: theories, advanced catalyst materials and system design, *Chem. Soc. Rev.* 48 (2019) 5658–5716.
- [27] S. Chen, D. Liu, T. Peng, Fundamentals and recent progress of photocatalytic nitrogen-fixation reaction over semiconductors, *Sol. RRL* 5 (2021), 2000487.
- [28] J. Zhao, Z. Chen, Single Mo atom supported on defective boron nitride monolayer as an efficient electrocatalyst for nitrogen fixation: a computational study, *J. Am. Chem. Soc.* 139 (2017) 12480–12487.
- [29] J. Cao, J. Li, W. Chu, W. Cen, Facile synthesis of Mn-doped BiOCl for metronidazole photodegradation: optimization, degradation pathway, and mechanism, *Chem. Eng. J.* 400 (2020), 125813.
- [30] C. Wang, Y. Zhang, W. Wang, D. Pei, G. Huang, J. Chen, X. Zhang, H. Yu, Enhanced photocatalytic degradation of bisphenol A by Co-doped BiOCl nanosheets under visible light irradiation, *Appl. Catal. B: Environ.* 221 (2018) 320–328.
- [31] Z. Sun, X. Yang, X. Yu, L. Xia, Y. Peng, Z. Li, Y. Zhang, J. Cheng, K. Zhang, J. Yu, Surface oxygen vacancies of $\text{Pd/Bi}_2\text{MoO}_6-x$ acts as "Electron Bridge" to promote photocatalytic selective oxidation of alcohol, *Appl. Catal. B: Environ.* 285 (2021), 119790.
- [32] G. Di, Z. Zhu, H. Zhang, Y. Qiu, D. Yin, J. Crittenden, Simultaneous sulfamethazine oxidation and bromate reduction by Pd-mediated Z-scheme $\text{Bi}_2\text{MoO}_6/\text{g-C}_3\text{N}_4$ photocatalysts: Synergetic mechanism and degradative pathway, *Chem. Eng. J.* 401 (2020), 126061.
- [33] K. Jing, W. Ma, Y. Ren, J. Xiong, B. Guo, Y. Song, S. Liang, L. Wu, Hierarchical Bi_2MoO_6 spheres in situ assembled by monolayer nanosheets toward photocatalytic selective oxidation of benzyl alcohol, *Appl. Catal. B: Environ.* 243 (2019) 10–18.
- [34] G. Zhang, D. Chen, N. Li, Q. Xu, H. Li, J. He, J. Lu, Fabrication of $\text{Bi}_2\text{MoO}_6/\text{ZnO}$ hierarchical heterostructures with enhanced visible-light photocatalytic activity, *Appl. Catal. B: Environ.* 250 (2019) 313–324.
- [35] J. Tang, Y. Ge, J. Shen, M. Ye, Facile synthesis of CuCo_2S_4 as a novel electrode material for ultrahigh supercapacitor performance, *Chem. Commun.* 52 (2016) 1509–1512.
- [36] Q. Meng, C. Lv, J. Sun, W. Hong, W. Xing, L. Qiang, G. Chen, X. Jin, High-efficiency Fe-Mediated Bi_2MoO_6 nitrogen-fixing photocatalyst: Reduced surface work function and ameliorated surface reaction, *Appl. Catal. B: Environ.* 256 (2019), 117781.
- [37] X. Li, H. Shi, S. Zuo, B. Gao, C. Han, T. Wang, C. Yao, C. Ni, Lattice reconstruction of one-dimensional mineral to achieve dendritic heterojunction for cost-effective nitrogen photofixation, *Chem. Eng. J.* 414 (2021), 128797.
- [38] Y. Xin, S. Wang, H. Yuan, T. Hou, W. Zhu, Y. Liu, Y. Yao, W. Zhang, S. Liang, L. Wang, Atomic-level insights into the activation of nitrogen via hydrogen-bond interaction toward nitrogen photofixation, *Chem* 7 (2021) 2118–2136.
- [39] T. Wang, J. Liu, P. Wu, C. Feng, D. Wang, H. Hu, G. Xue, Direct utilization of air and water as feedstocks in the photo-driven nitrogen reduction reaction over a ternary Z-scheme $\text{SiW}_6\text{Co}_3/\text{PDA/BWO}$ hetero-junction, *J. Mater. Chem. A* 8 (2020) 16590–16598.
- [40] T. Wang, C. Feng, J. Liu, D. Wang, H. Hu, J. Hu, Z. Chen, G. Xue, Bi_2WO_6 hollow microspheres with high specific surface area and oxygen vacancies for efficient photocatalysis N_2 fixation, *Chem. Eng. J.* 414 (2021), 128827.
- [41] X. Sun, D. Jiang, L. Zhang, S.M. Sun, W.Z. Wang, Enhanced nitrogen photofixation over LaFeO_3 via acid treatment, *ACS Sustain. Chem. Eng.* 5 (2017) 9965–9971.
- [42] X. Gao, L. An, D. Qu, W. Jiang, Y. Chai, S. Sun, X. Liu, Z. Sun, Enhanced photocatalytic N_2 fixation by promoting N_2 adsorption with a co-catalyst, *Sci. Bull.* 64 (2019) 918–925.
- [43] J. Yang, Y. Guo, R. Jiang, F. Qin, H. Zhang, W. Lu, J. Wang, J. Yu, High-efficiency "working-in-tandem" nitrogen photofixation achieved by assembling plasmonic gold nanocrystals on ultrathin titania nanosheets, *J. Am. Chem. Soc.* 140 (2018) 8497–8508.
- [44] S. Gao, R. Wu, M. Sun, M. Guo, D.B. DuBois, S. Chen, H. Ji, C. Wang, Q. Wang, High-performance nitrogen photofixation by $\text{Bi}_2\text{Sn}_2\text{O}_7$ nanoparticles enriched with oxygen vacancies, *Appl. Catal. B: Environ.* 324 (2023), 122260.
- [45] P. Li, Z. Zhou, Q. Wang, M. Guo, S. Chen, J. Low, R. Long, W. Liu, P. Ding, Y. Wu, Visible-light-driven nitrogen fixation catalyzed by $\text{Bi}_5\text{O}_7\text{Br}$ nanostructures: enhanced performance by oxygen vacancies, *J. Am. Chem. Soc.* 142 (2020) 12430–12439.
- [46] X. Liu, Y. Luo, C. Ling, Y. Shi, G. Zhan, H. Li, H. Gu, K. Wei, F. Guo, Z. Ai, Rare earth La single atoms supported MoO_3-x for efficient photocatalytic nitrogen fixation, *Appl. Catal. B: Environ.* 301 (2022), 120766.